Large coherent structures in fractal jets

Gioacchino Cafiero[1,*], Stefano Discetti[2], Tommaso Astarita[1]

[1]Department of Industrial Engineering, University of Naples, Naples, Italy
[2]Departamento de Bioingenierìa e Ingenieria Aeroespacial, Universidad Carlos III de Madrid, Leganés, Spain
*corresponding author: gioacchino.cafiero@unina.it

Abstract A flow field investigation of a circular air jet equipped with a fractal insert is carried out. The analysis in the mid plane of the nozzle is performed to characterize the streamwise evolution of the jet with and without the insert by means of 2D-2C Particle Image Velocimetry (PIV). Moreover, the large coherent structures that dominate the flow field in presence of fractal grid (FG) and in the case of jet without turbulator (JWT) are investigated using 3D-3C Tomographic PIV. In all the experiments the Reynolds number based on the nozzle exit section diameter d is equal to about 15,000. For planar PIV experiments, as the fractal grid unsettles the axial symmetry of the flow field, two planes are investigated respectively aligned with the x axis direction and tilted of 45° with respect to it. On the other hand, for the JWT case only the symmetry plane of the nozzle is investigated. It is demonstrated that the presence of the grid enhances the entrainment rate of the jet, thus leading to a higher scalar transfer. This effect sums up to the turbulent kinetic energy production which is characteristic of FGs. In the case of shear-less flows Hurst and Vassilicos have shown a peculiar profile of the velocity fluctuation along the wind tunnel axis, characterized by an elongated production region, a peak which can be located as a function only of grid geometric parameters and a fast decay. In this work it is shown how the penetration of the shear layer interacts with the turbulence decay.
The high energy containing ring vortices are replaced by couples of counter-rotating streamwise vortices as highlighted via the Tomo-PIV experiments. Although less energetic, these structures result to be more stable than the ring vortices and as a consequence, they lead to an enhancement of the entrainment rate and of the scalar transfer of the jet, as demonstrated via the streamwise PIV data. The application of the POD analysis to the 3D flow field reveals the presence of the shedding of a "Karman-like" wake which is shed by the largest grid bar. This unsteady effect sums up to the streamwise vortices which can be detected into the time averaged flow field.
Keywords: fractal jets, free jets, streamwise vortices

1 Introduction

The study of free turbulent jets has been one of the main topics in the fluid dynamics research of the last few decades. Their importance in countless applications, such as aeronautical engines, ignition process in combustion chambers, cooling of electronic devices to cite some, stimulated numerous investigations. Particular attention has been devoted to the study of round jets, i.e. jets issuing through a nozzle with circular cross section for their intrinsic modeling and manufacturing simplicity.
The mean flow field features of round turbulent jets is widely described into the literature. [1] settled many aspects of round turbulent jets, defining the main properties and characteristics of such flow field as the extent of the potential core (i.e. the region where the axial velocity of the jet remains equal to the exit one) which penetrates for about $6d$, being d the nozzle exit section diameter; he also defined the minimum distance along the nozzle axis such that the velocity profile becomes self-similar. The organization of the large coherent structures of circular jet flows has been widely detailed into the literature. [2] deeply investigated the fluid field features of round jets using flow visualization techniques; they found that vortical axisymmetric structures arise due to the interaction of the jet shear layer with the quiescent ambient air,. They also documented that the characteristic Strouhal number ($Sr = fd/V_j$, being f the shedding frequency of the structures and V_j the jet exit velocity) of the large-scale vortex puffs, then referred to as ring vortices for their azimuthal coherence, is about equal to 0.72. The mechanism that leads to the formation of the ring vortices has been demonstrated to be associated to the growth of azimuthal disturbances within the jet shear layer, i.e. the Kelvin-Helmholtz instability [3], [4]. The toroidal vortices grow maintaining the axial symmetry up to a relatively short streamwise distance from the nozzle exit section (about 4d). Beyond that point, the relative effect of vortex induction leads to the pairing phenomenon [2], [5].
Since the development and the evolution of coherent structures regulates the entrainment process [6] i.e. the mixing of the external air with the jet core, the understanding of the evolution of these energy-containing features is of paramount importance. This led to the study of several solutions to enhance the engulfment of

air from outside the jet core towards the inside. Among the others, non-circular geometries like square [7], tabbed [8], daisy [9], cruciform [10] or chevron nozzles [11], which from one side stimulate the production of streamwise vortices and from the other interact with the generation of the annular structures typical of axisymmetric jets, are commonly applied solutions. The introduction of an upstream swirl component to the main flow [12], [13]; the use of fluidic devices like naturally precessing jets [14]; pulsating jets (synthetic jets [15]) have also been widely investigated.
Other passive methods are also commonly used to enhance the scalar transfer of jets. The introduction of mesh screens [16], [17] or perforated plates [18] either in correspondence or in the vicinity of the nozzle exit, from one side interacts with the formation of the large structures of the flow field and from the other causes a strong turbulence enhancement. Recently, Cafiero et al [19] proposed the use of fractal grids (i.e. grid with a pattern repeated at increasingly smaller scales) to enhance the heat transfer capabilities of circular impinging jets. They compared the performances of impinging jets at relatively short nozzle exit section to plate distances equipped with square fractal grids, regular grids and jet without turbulators. They showed that a very strong enhancement of the heat transfer rate can be achieved using fractal jets, obtaining in particular an improvement in terms of Nusselt number up to 63% in the stagnation region with respect to a regular grid under the same power input. This strong enhancement was addressed to the formation of streamwise structures and to the turbulence intensity enhancement past the fractal grid. However, several interrogatives were left open and demanded a flow field investigation to relate the observed features to those more documented of fractal grids in free-shear flow and to explain the significant discrepancies. In the case of free-shear flow, Hurst & Vassilicos [20] studied the turbulence produced by fractal grids with different patterns (square, "I"-shaped and cross-shaped). One of the main findings was that, differently from what happens for regular grids (RGs), where a very intense peak in the turbulence intensity profile is located right beyond the grid, in the case of fractal grids (FGs) the production region is significantly larger under the same blockage ratio and the location of the maximum can be tuned as a function of only geometric parameters of the grid. In particular they observed that the location of the maximum can be estimated as $x_{peak} \approx 0.45\ (L_0^2)/t_0$, being L_0 and t_0 respectively the length and the thickness of the first grid iteration [21]. In fact, from a geometric argument based on Prandtl mixing length theory, considering that the turbulence intensity builds up as a function of the interaction between the wakes shed by the grid bars, in the case of a RG all the wakes meet at the same streamwise location; on the contrary, in the FG case wakes generated by bars of different size and spacing will meet at different positions. While the wakes shed by the largest square composing the grid should meet at approximately L_0^2/t_0, the "anticipated" turbulence peak was addressed to the effect of interactions of the wakes of the smaller iterations, which meet upstream of it. A fast decay of the turbulent kinetic energy has been observed beyond the local maximum [21]. Whereas this behavior is well assessed for free-shear flows, to the authors' knowledge there is no work that attempts to characterize the turbulence produced by FGs in a jet flow, thus taking into account the effect of the growing shear layers on the grid turbulence. In addition to this, recently there is a growing interest in the use of fractals for mixing improvement and turbulence enhancement, such as fractal cross grids in opposed jets to promote the turbulent strain in combustion applications [22]; Kinzel et al [23] used fractal cross grids to generate turbulence with sufficiently high intensity to investigate the effect of rotation on high intensity shear-free turbulence; Nedic et al [24] proposed to use fractal spoilers to reduce the low frequency aerodynamic noise associated to the recirculating flow.
In this work the flow field characterization of a free round jet equipped with a square fractal grid is carried out by means of Particle Image Velocimetry (PIV). A comparison with the flow field features of the jet without turbulator (JWT) is presented. Moreover, the interaction of the turbulence produced by the grid with the penetration of the growing shear layer across the jet potential core is discussed. Fully three dimensional measurements by means of Tomographic PIV (Tomo-PIV) are also carried out in order to describe the coherent structures that dominate the flow field in the FG and JWT cases. The main differences are pointed out and related to the higher mixing efficiency achieved by FGs.
To the authors' knowledge, this represents the first effort in the literature to define and characterize fractal jets from the fluid dynamic standpoint. The wide interest on application of fractal grids in several fields and shear flow applications makes them particularly appealing and worth of investigation.
In the next section, the experimental setup will be described in detail. Then the main results will be widely addressed in sections 3-4. Finally, the conclusions will be drawn in the last section.

2 Experimental procedure

The experiments are carried out in the air jet facility at the University of Naples Federico II. The air is collected from the ambient using a centrifugal blower; an inverter is used to regulate the input shaft power. The flow rate is measured using a rotameter. The air passes through a radiator to control in temperature the blown fluid. The air is then collected within a stagnation chamber (internal diameter and length equal to $3d$ and $20d$, respectively) located downstream of the nozzle to reduce the effects of fluctuations and biases from the feeding circuit. Furthermore, two honeycomb grids are located within the chamber in order to reduce the turbulence level due to large flow structures. The working fluid passes then through a short-pipe round nozzle ($6.2d$ long) and a terminating cap in correspondence of the nozzle exit section where the grid is located (see Figure 1c for details). The final part of the air circuit (stagnation chamber and nozzle) is arranged on a traversing stage (as illustrated in Figure 1a-b), which ensures the movement of the nozzle along its own axis with accuracy of 0.1mm.
The flow is seeded with olive oil particles (about 1μm diameter) generated by a Laskin nozzle. The mixing between the working fluid and the seeding particles occurs in a reservoir located upstream of the stagnation chamber.
The light source is a Quantel Evergreen laser for PIV applications (532nm wavelength, 200mJ/ pulse, <10ns pulse duration) with an exit beam diameter of about 5mm. The laser beam is enlarged using a bi-concave lens with negative focal length (-50mm); it is then adjusted in thickness using a second bi-convex lens with positive focal length (100mm), in order to ensure a uniform illumination along the depth direction. Finally a cylindrical lens (focal length 100mm) is used to enlarge the laser in the plane orthogonal to the optical axis of the camera.
In the Tomo-PIV experiments the optical arrangement is slightly different with respect to the planar PIV one: the second spherical lens has a focal length equal to 200mm; moreover, a pinhole is used in order to cut the peripheral region of the laser source. Two different sets of Tomo-PIV experiments are carried out (see Figure 1). A first set (here and in the following referred to as SET-A) where the crosswise flow field is investigated, with the track of the laser volume being parallel to the XZ plane (see Figure 1c for the reference system). In this case the illuminated region extends for about 10mm along the Y direction (i.e. along the nozzle axis) and for 30mm along the X and Z direction. A second set (here and in the following referred to as SET-B) is instead devoted to highlight the streamwise organization of the flow field. The laser volume is in this case directed along the YZ plane and such that one side of the central square of the fractal grid belongs to the illuminated region. The extent of the laser volume is of 60mm along the Y direction, 30mm along the Z direction and 10mm along the X direction.
The PIV imaging system is made of one Andor sCMOS 5.5Mpixels camera (camera 3 in Figure 1b) equipped with Nikon objective with focal length 50mm; four Andor sCMOS cameras (camera 1-4 in Figure 1a-b) in Scheimpflug arrangement equipped with Tokina 100mm macro objectives are instead used for the tomographic PIV experiments. The cameras are co-planar and subtend a solid angle of about 60°.
Both for PIV and Tomo-PIV experiments the flow rate is regulated using a rotameter in order to obtain a Reynolds number (based on the nozzle exit section diameter d) equal to Re=15,000. The resulting bulk velocity is then $V_j = 10.5 m/s$ and this will be the value used to normalize all the quantities in the following of the paper (unless otherwise stated).
In the PIV experiments 2,000 snapshots are captured. The imaged area extends for about 3x11.5 d in the XY plane, resulting in a spatial resolution of about 10.5 pix/mm, i.e. 210pix/d. The image interrogation is performed using a window size of 24x24pixels, 75% overlap and Blackman filtering window within the correlation process to tune the spatial resolution [25].
The calibration procedure for the Tomo-PIV experiments is performed by taking images of a target (black dots on white background, 5mm pitch in the X,Z directions) moved through the measurement volume in seven different locations using a translational micrometric stage. The maximum calibration error is of the order of 0.5pixels. A self-calibration [26],[27] procedure is then carried out in order to further correct the location of the laser volume using the scattering particles. This leads to a reduction of the calibration error down to 0.03pixels.
The imaged area for the SET-A extends for 1.5d x 1.5d in the two directions orthogonal to the nozzle axis (namely X and Z) and about 0.45d along the nozzle axis (Y), thus resulting in a digital resolution of 50 voxels/mm in the middle of the interrogation volume. For the SET-B the imaged area is of about 3d along the nozzle axis (Y), 1.3d in the direction aligned to the grid bar (Z) and 0.35d in the third direction (X), thus

leading to a digital resolution of 36voxels/mm in the middle of the interrogation volume. For the SET-A, a sequence of 1,000 couples of images is acquired for each of the two investigated cases (FG and JWT). In the SET-B only the FG case is considered, still on a dataset of 1,000 samples.

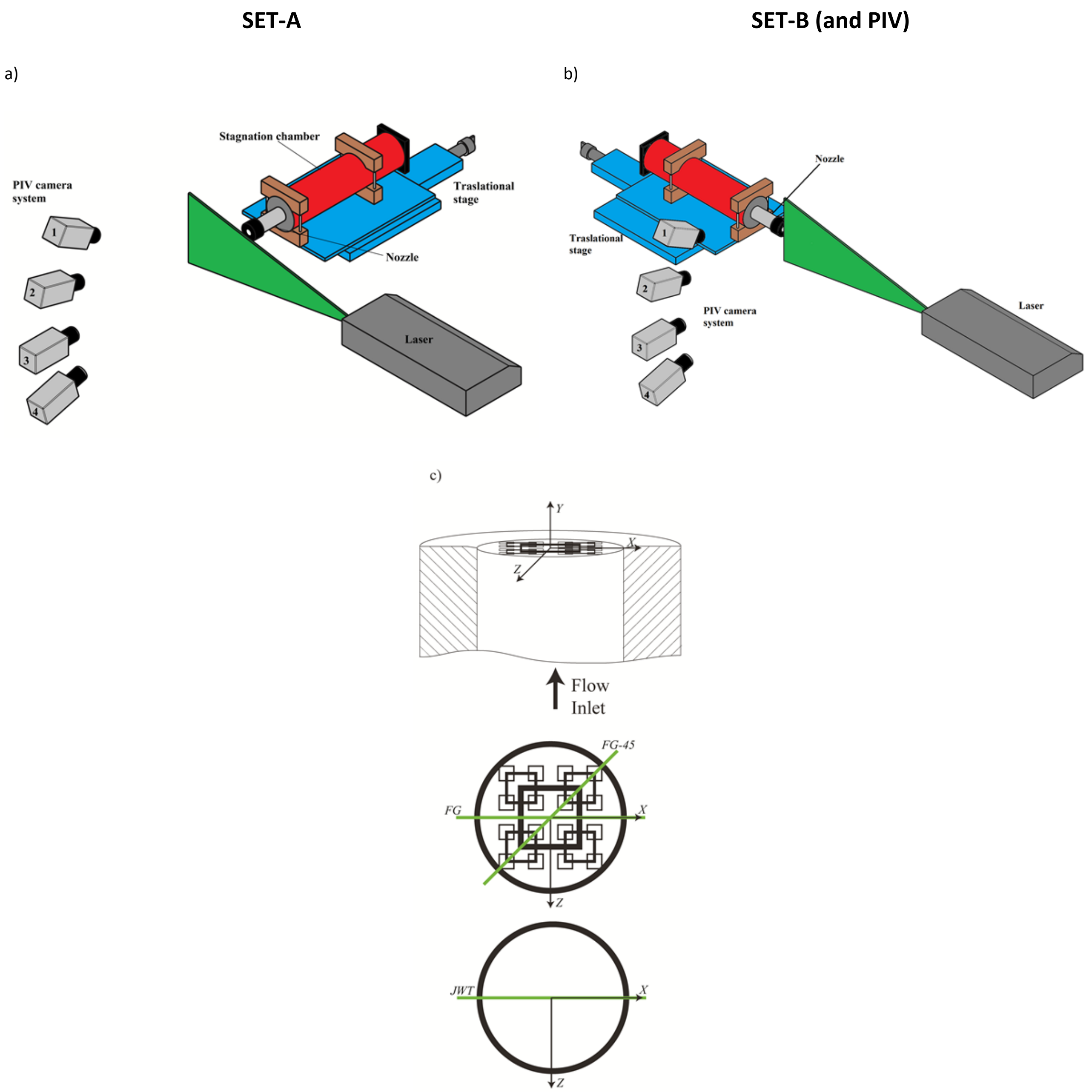

Fig. 1 Experimental apparatus layout for Tomo-PIV experiments SET-A (top-left, a) and SET-B (top-right, b); for PIV experiments, the setup b) is representative of the real conditions, considered that only camera 3 is used and the laser volume is reduced to a laser sheet 0.5 mm thick. c) Detail of the grid located at the nozzle exit section with indication of the measurement plane for PIV. FG refers to the case of laser aligned to XY plane; in the FG-45 the laser is instead rotated around the Z axis of 45° with respect to the previous case (i.e. aligned to the diagonal of the largest grid iteration).

A pre-processing is applied to the raw images in order to reduce the background noise. The pre-processing consists in: temporal minimum image subtraction, in order to limit the effect of laser reflections within the

flow field; a sliding minimum subtraction over a kernel of 7x7 pixels; a sharpening and Gaussian filtering over a 7x7 pixels in order to smooth the particles shape.
The reconstruction algorithm used for both SET-A and SET-B is the same. The 3D volume is reconstructed from the pre-processed images using 5 MART iterations [28], 1 MTE iteration [29], and 3 final MART iterations. During the iterative reconstruction with MART a non-isotropic Gaussian smoothing is applied on a 3x3x1 kernel (SFIT, [30]) in order to reduce the artifacts of the reconstruction due to particles elongation along the depth direction in the reconstructed volumes. In order to check the quality of the reconstruction the signal to noise ratio defined as the reconstructed particles intensity inside the illuminated area versus that reconstructed outside is calculated. In the present experiment, the intensity of the laser is uniformly distributed across the volume which extends in the SET-A for about 450 voxels in depth (thus corresponding to about 9mm) and for about 260 voxels in depth (thus corresponding to about 7mm) in the SET-B, leading to a S/N ratio of about 2 for both cases.
In the SET-A the reconstructed volume is interrogated using a 3D cross-correlation algorithm based on a final interrogation volume of 48x48x48voxels (0.96x0.96x0.96 mm^3), 75% overlap. The resulting vector pitch is 0.24m. In the SET-B the final interrogation volume is slightly larger than the previous case, namely 64x64x64voxels (1.77x1.77x1.77 mm^3), 75% overlap. The vector pitch is then 0.44mm. The cross-correlation process is performed with an efficient algorithm based on sparse matrices and minimization of redundant calculations when using overlapping windows [31].

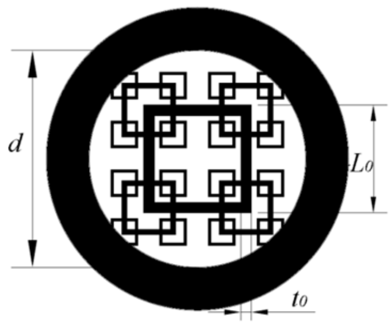

Fig. 2 Fractal grid insert representation

A sketch of the fractal insert is reported in Figure 2. The insert is made of a 0.5mm thick aluminum foil; the fractal structure is shaped by laser cutting. The square pattern is repeated at three different scales (referred to as iterations). The length L_0 and the thickness t_0 of the first iteration are equal to 10mm and 1mm, respectively. At each iteration j the length L_j and the thickness t_j are halved, i.e. $L_j = L_0 R_L^j$ and $t_j = t_0 \; R_t^j$, with $R_L = R_t = 1/2$. For this grid the ratio between the largest and the smallest bar thickness (i.e. the thickness ratio t_r, identified as a significant scaling parameter by Hurst & Vassilicos [20]) is equal to 4. The blockage ratio of the grid is equal to 0.32.

3 PIV Results

The contour representation of the mean axial velocity obtained by averaging 2,000 PIV samples is reported in Figure 3. It is worth to explicitly notice that, when referring to the analysis in the plane aligned with the X axis direction, it is used the FG abbreviation; whilst when referring to the plane tilted of 45° with respect to the X axis (in the XZ plane), FG-45 is used (see Figure 1c).

The main differences between the two presented cases can be spotted in the vicinity of the nozzle exit section. The round jet without turbulator (whose nozzle has been extensively detailed by the authors in a previous work [14]) is characterized by an initial region which extends up to Y/d=1.5 where the fluid issued through the nozzle is still developing. In this region the shearing effect of the surrounding air is still limited and the shear layer thickness is approximately constant. However, the azimuthal disturbances are growing in amplitude and they reach their maximum at Y/d=1.5, where the shear layer becomes unstable and starts to spread [2], [6].

Beyond that point, the jet spreads almost linearly entraining fluid from the surrounding quiescent ambient. In good agreement to what shown by other authors (see [1], [2], [11] among the others), along the jet centerline the velocity remains equal to the exit one for a region that penetrates for about 4.5d, typically referred to as "potential core" (see Figure 4).

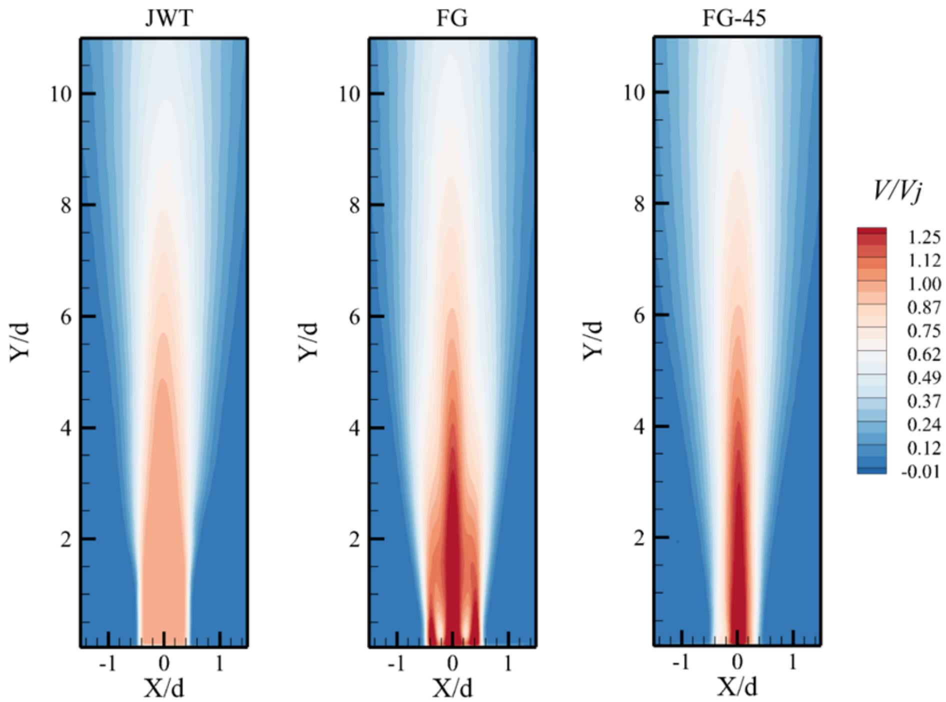

Fig. 3 Mean axial velocity contour representation in the JWT case (left) FG case (center) and FG-45 case (right)

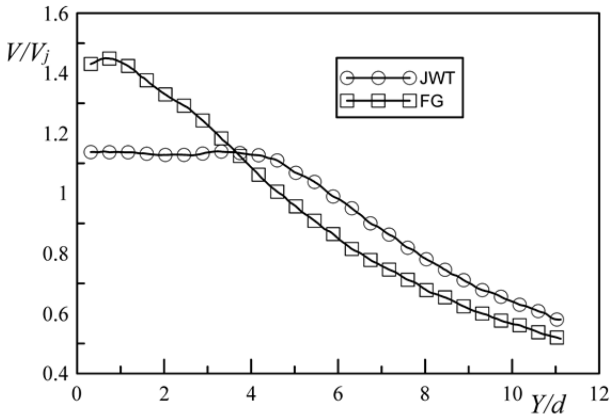

Fig. 4 Axial velocity decay along the nozzle centerline for the JWT(□), FG(□) cases

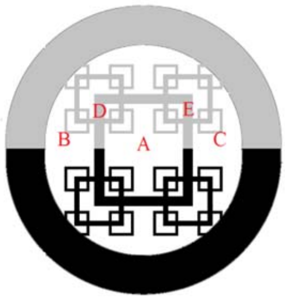

Fig. 5 Identification of the main regions in the FG case

The FG case is instead characterized by three regions of large values of the axial velocity respectively located in correspondence of the central (and largest) iteration (region A, Figure 5) and of the "holes" between the grid bars and the edges of the grid (respectively regions B and C, Figure 5). Moreover, the presence of the grid is also reflected into two regions of defect of velocity located in correspondence of the wake of the central iterations grid bars (regions D and E, Figure 5). The hornet-shape is soon lost due to turbulent diffusion beyond Y/d=2, where only the inner jet persists. Beyond Y/d=4, the effect of the two outer jets cannot be perceived on the mean velocity profile.

In the FG case, the jet spreading starts immediately beyond the grid, differently from what observed in the JWT case. This effect has to be addressed to the blockage imposed by the wakes of the largest iteration of the fractal grid on the two lateral jets.

The FG-45 case presents a very strong central jet, whose radial extension is reduced with respect to the FG case due to the effect of the secondary iterations of the grid. At sufficiently large distances from the nozzle exit section, the effect of the grid on the mean velocity is negligible and the FG and FG-45 cases match. This aspect can be further investigated looking at the axial velocity profiles (Figure 6) extracted at different streamwise locations (Y/d={0.25,5.5,11}). First, it is interesting to notice that, the velocity profiles are non-dimensionalized with respect to the bulk velocity as already outlined in the previous sections. The JWT case must then be compared to an average of the two cases with the grid insert, since the presence of the fractal turbulator unsettles the axial symmetry of the jet. At large distances from the nozzle exit section, it is possible to see how the three cases are getting closer and closer, suggesting that the effect of the fractal grid insert is being smeared out.

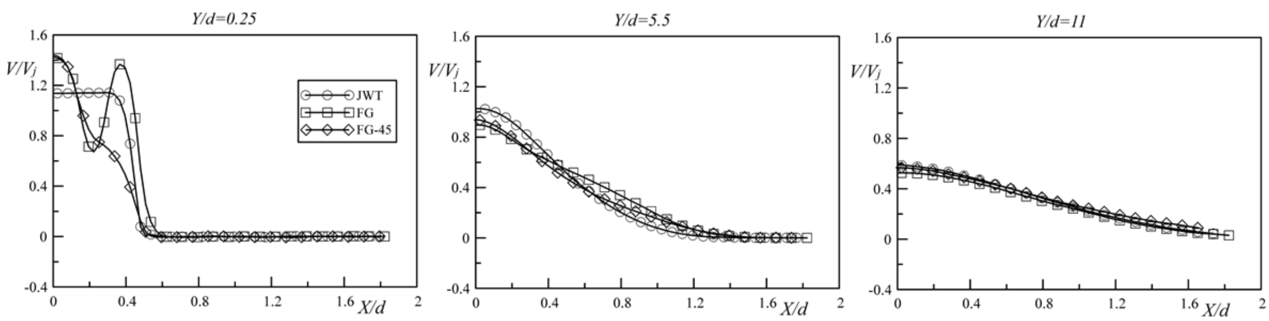

Fig. 6 Axial velocity profiles for the JWT(□), FG(□) and FG-45(□) cases at Y/d=0.25 (left), Y/d=5.5(center) and Y/d=11 (right)

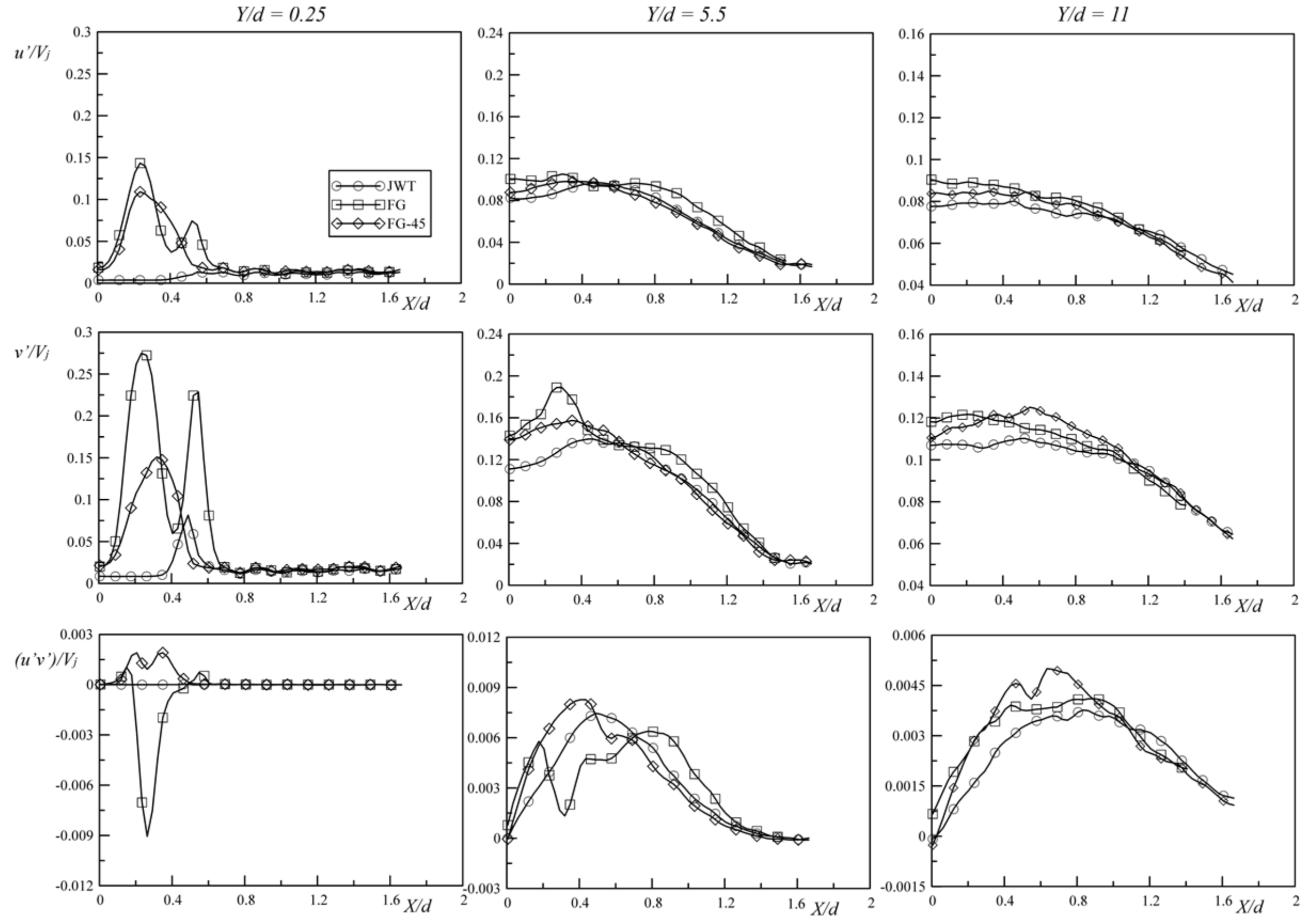

Fig. 7 Radial (first row) and axial (second row) velocity fluctuations and planar Reynolds stress (third row) for the JWT(□), FG(□) and FG-45(□) cases at Y/d=0.25 (left), Y/d=5.5 (center) and Y/d=11 (right)

Figure 7 represents the root mean square (rms) of the axial v' and radial u' velocity fluctuations along with the Reynolds stress u'v' for the three investigated cases at three different locations along the nozzle axis (Y/d={0.25,5.5,11}). It is possible to spot a striking difference between the JWT case and FG, FG-45 cases, especially near the nozzle exit section. At Y/d=0.25 the effect of the fractal grid reflects in the presence of an intense peak in both the axial and radial velocity fluctuations; it is interesting to notice that for the FG-45 case the effect of the merging wakes that detach from the grid iterations is combined to the one related to the shear layer, whose width is definitely broader than the FG case. The JWT case is characterized by a peak located in correspondence of the jet shear layer for the axial fluctuation, whilst it is quite flat in the radial direction. The planar component of the Reynolds stress highlights even more the differences between the three cases. The shear produced by the largest grid iteration causes a very intense minimum in the u'v' distribution. This is indicative of negative radial fluctuations (inward flow) systematically coupled with positive axial fluctuations (ejections in the bars wake) and vice-versa, which is consistent with the picture of an unsteady spreading wake. Moving farther downstream, it is interesting to notice that the FGs cases are slowly adjusting to the JWT case, losing memory of the presence of the grid. However, this effect is quicker in the FG-45 case; this must be addressed to the fact that the flow field in this case results to be strongly influenced by the blockage of the secondary iterations of the grid, but only in the very vicinity of the nozzle exit section. Due to the large momentum difference between the central jet and the jets issuing through the holes of the secondary iterations it was foreseeable that the jets interactions would be concentrated and resolved in few diameters beyond the grid.

Figure 8 underlines the main differences between the turbulent kinetic energy produced in the JWT and FG cases along the jet centerline. Whilst the JWT case is characterized by an initial plateau and a subsequent increment due to the penetration of the jet shear layer, the FG case presents a turbulence production region past the grid due to the interaction of the wakes of the grid bars. According to Mazellier and Vassilicos [21] in the case of free-shear wake of a fractal grid a local maximum should be identified at about $0.45L_0^2/t_0$. For the used grid, this would turn into a streamwise distance of about 2.25d. Beyond that point, in their investigation a steep turbulent energy decay was spotted, which led to the controversial discussion on whether it is exponential or modeled by the classical power law of the regular grids, or an hybrid between the two solutions [32], [33]. Differently from the case investigated by Mazellier & Vassilicos [21] the local maximum in the turbulent kinetic energy profile is followed by another production region due to the penetrating shear layer.

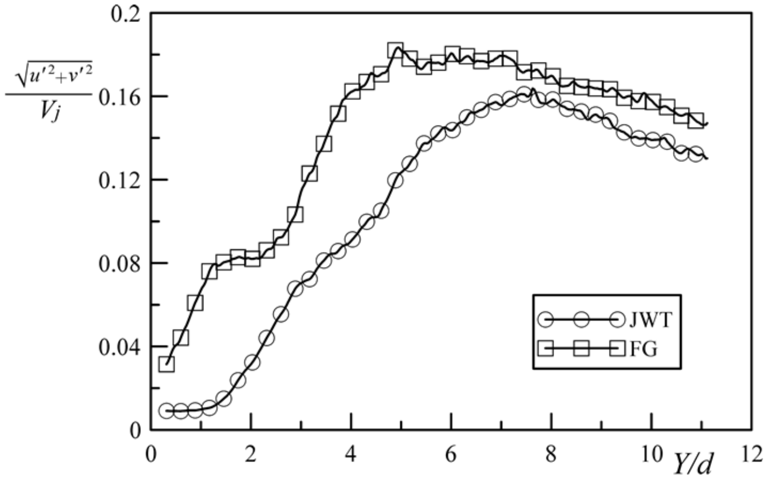

Fig. 8 Turbulent kinetic energy profile along the jet centerline for the JWT(○) and FG(□) cases

In fact, as moving further downstream, the latter effect sums up to the production due to the fractal grid. The observed plateau for 1.8<Y/d<2 can be addressed to this interaction. Indeed, the turbulence injected by the shear layer balances out the decaying turbulence produced by the grid. In addition to this, the local maximum of the turbulent kinetic energy anticipates the one predicted by Mazellier & Vassilicos [21] in a free-shear case. This aspect must be addressed to the growing shear layer which "pushes" the wakes towards the nozzle axis, causing an anticipated merging of the wakes of the main iteration.

4 Volumetric PIV results

Due to the strong 3D features of the flow field, targeted 3D experiments can shade some light on the organization of coherent structures. The mean flow field organization, calculated over 1,000 samples for the FG (a) and JWT (b) case is reported in Figure 9. For the FG case (a), the hornet shaped axial velocity profile as highlighted in the PIV experiments reflects in the present case into a cross-shaped iso-surface of $V\ /\ V_j\ =1$ (color-coded in translucent green) which embraces the central jet. As already outlined when presenting the PIV results, this peculiar shape must be addressed to the jets issuing through the regions B, C, as indicated in Figure 5. Moreover, the iso-surface of axial velocity $V/V_j = 1.6$ is reported in orange to underline the central jet (corresponding to region A). In terms of turbulence production, besides the effect of the shear layer due to the interaction of the quiescent air with the issuing jet, for the FG case the turbulence generated by the grid deserves consideration. The iso-surface of turbulent kinetic energy (tke) normalized with respect to the bulk velocity of the jet V_j is also reported in Figure 9 (translucent grey, $tke/V_j = 0.074$). The four structures indicated in translucent grey are associated to the turbulence produced by the bars of the first iteration. Cafiero et al [19] conjectured that the streamwise vorticity generation due to the grid corners, along with the larger axial velocity values of the jets issuing through the grid iterations, were responsible of the strong gap between the FG and JWT in terms of scalar transfer efficiency when using impinging jets equipped with fractal grids with the aim of enhancing their heat transfer efficiency. The turbulent kinetic energy distribution is consistent with this picture. Further evidence can be extracted by observing the iso-surfaces of normalized axial vorticity $\omega_y\, d/V_j$ reported in Figure 9, which reveal the presence of couples of counter-rotating vortices that evolve in the streamwise direction. They must be addressed to the interaction of the fluid issuing through the regions B, C with the grid iterations. The production of these energy containing structures which evolve in the streamwise direction are responsible of the increment of the entrainment rate as already shown by Grienstein [6].

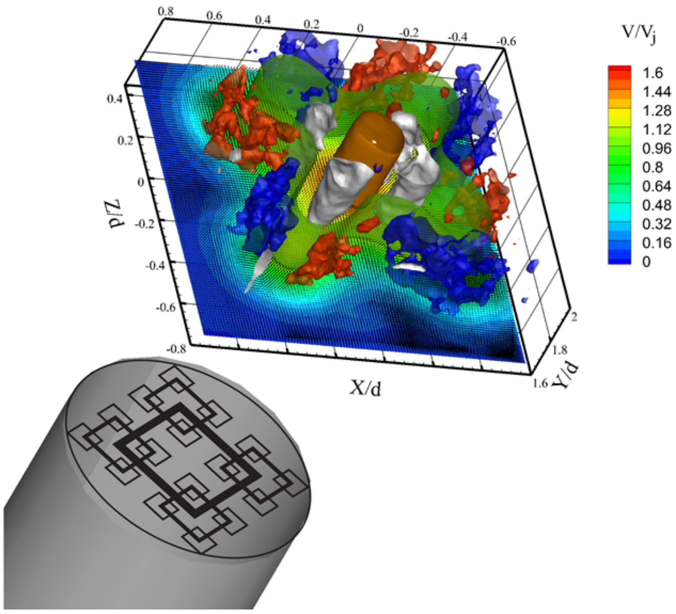

Fig. 9 Mean flow field features for the SET-A: Iso-surfaces of axial velocity $V/V_j = 1.6$ (orange) and $V/V_j = 1$ (translucent green); Iso-surfaces of axial vorticity $\omega_y d/V_j = 0.65$ (red) $\omega_y\ d/V_j$=-0.65 (blue); Iso-surface of $tke/V_j = 0.074$ (translucent grey). Contour representation of the axial velocity in the XZ plane along with vector plot

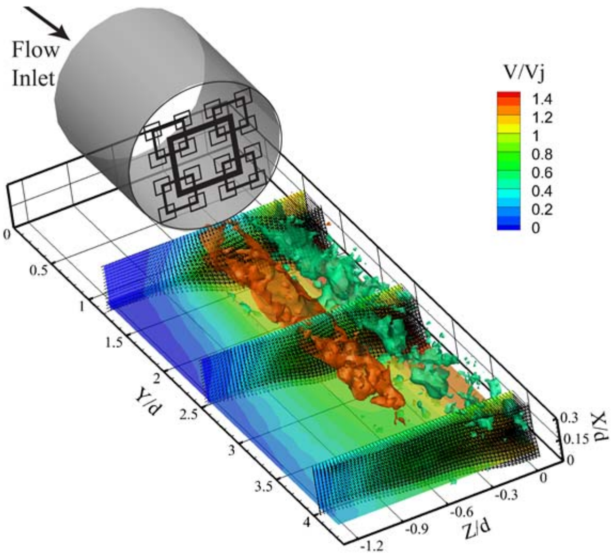

Fig. 10 Mean flow field features for the SET-B; iso-surface of axial vorticity $\omega_y\ d/V_j = 0.65$ (red) and $\omega_y\ d/V_j = -0.15$ (green). Contour representation of the axial velocity both onto the YZ (X/d=0) and XZ (Y/d={1.2,2.5,4}) planes.

These streamwise structures have larger penetration and lifetime than the vortex rings generated in the shear layer, and might be largely responsible of the heat transfer enhancement observed by Cafiero et al [19] in impinging fractal jets.
The SET B of experiments, in this sense, can add some useful information on the penetration of the streamwise vorticity along the centerline. Additionally, it provides further insight in the interaction between primary and secondary iterations.
The ensemble averaged flow field for the SET-B is reported in Figure 10. The contour representation of the axial velocity is illustrated in the X/d=0 and Y/d={1.2,2.5,4} planes. The normalized axial vorticity iso-surface $\omega_y\ d/V_j = 0.65$ corresponds to the one represented in Figure 9, i.e. to the vortex generated because of the interaction of the flow with the grid in correspondence of region B. However, it may be argued that as fractal grids cover inherently multiple scales, as a function of the scale of the grid iteration the flow can be characterized by the presence of different structures. Indeed, the interaction of the second iteration of the jet

with the grid bars and the secondary grid iterations causes the presence of a streamwise vortex, which rotates in the opposite direction with respect to the previous one (represented with the iso-surface $\omega_y\, d/V_j = -0.15$). It must be noticed that, for a symmetry argument, another vortex characterized by an opposite value of axial vorticity ($\omega_y\, d/V_j = 0.15$) will be generated in correspondence of the region between the top right corner of the grid and the largest grid iteration.

4 Discussion and conclusions

In the present work the experimental analysis of a round jet equipped with a square fractal grid is carried out. The characterization of the streamwise organization of the mean flow field is performed using 2D2C-PIV along two different planes: the mid-plane of the nozzle and a plane tilted of an angle equal to 45° with respect to it (respectively FG and FG-45 case, see Figure 1). A comparison with the well assessed flow field of round jet without turbulator (i.e. without the presence of the fractal grid) is presented. The main differences introduced by the presence of the grid insert rely in the vicinity of the nozzle exit section. From one side, in the FG case the grid insert unsettles the axial symmetry of the round nozzle, thus leading to a “hornet-shaped” velocity profile with three strong jets issued through the grid iterations (regions A, B and C in Figure 5); the FG-45 case is instead characterized by a strong central jet (which width is about equal to 0.5d) since the secondary iterations of the fractal grid cause a local blockage to the issuing fluid, then leading to a strong reduction of the axial velocity.
In the FG case, the investigation of the turbulence intensity profile along the nozzle axis leads to some interesting differences with respect to the case of free-shear flow; in fact, the location of the peak in the turbulence intensity profile which in the case of free-shear flow should be located at about Y/d≈2.25 anticipates; this effect must be addressed to the growing shear layer which triggers an asymmetry in the spreading of the fractal grid wakes.
As a consequence of the inherent three-dimensionality of the flow field in the FG case, volumetric PIV measurements are carried out in order to provide a clearer view of the large scale organization of the flow field. In particular, a first set of experiments (referred to as SET-A) gives the evidence of the presence of couples of counter-rotating streamwise vortices which embrace the cross-shaped jet. They are associated to the azimuthal disturb induced by the fractal grid in a similar fashion to what observed in other non-circular jets such as tabbed and chevron. However, differently from the cited cases, due to the multi-scale topology of the flow field (being the fractal grid inherently multi-scale), the presence of streamwise vortices with different characteristic dimensions is experienced. In particular, different structures are convected down to different streamwise locations along the nozzle axis depending on the dimensions of the source (i.e. the grid bar thickness).

References

[1] Abramovich (1963) The theory of turbulent jets. The M.I.T. Press, Cambridge, Massachusetts.

[2] Crow SC and Champagne FH (1971) Orderly structure in jet turbulence. Journal of Fluid Mechanics 48, 547.

[3] Bradshaw P, Ferriss DH and Johnson RF (1964) Turbulence in the noise producing region of a circular jet. Journal of Fluid Mechanics 19:591

[4] Becker HA, Massaro TA (1968) Vortex evolution in a round jet. Journal of Fluid Mechanics 31:435.

[5] Winant CD, Browand FK (1974) Vortex pairing: The mechanism of turbulent mixing layer growth at moderate Reynolds number. Journal of Fluid Mechanics 63:237.

[6] Grinstein FF (2001) Vortex dynamics and entrainment in rectangular free jets. Journal of Fluid Mechanics 437: 69-101.

[7] Gutmark EJ and Grinstein FF (1999) Flow Control with noncircular jets. Annual review of Fluid Mechanics 31:239-272.

[8] Gao N, Sun H, Ewing D (2003) Heat transfer to impinging round jets with triangular tabs. International Journal of Heat and Mass Transfer 46(14): 2557-2569.

[9] El Hassan M, Meslem A (2010) Time-resolved stereoscopic particle image Velocimetry investigation of the entrainment in the near field of circular and daisy-shaped orifice jets. Physics of Fluids 22: 035107.

[10] El Hassan M, Meslem A, Abed-Meraim K (2011) Experimental investigation of the flow in the near-field of a cross-shaped orifice jet. Physics of Fluids 23:045101.

[11] Violato D and Scarano F (2011) Three-dimensional evolution of flow strucutres in transitional circular and chevron jets. Physics of Fluids 23: 124104.

[12] Syred N (2006) A review of oscillation mechanisms and the role of the precessing vortex core (PVC) in swirl combustion systems. Progress in Energy and Combustion Science 32: 93-161.

[13] Ceglia G, Discetti S, Ianiro A, Michaelis D, Astarita T and Cardone G (2014) Three-dimensional organization of the flow structure in a non-reactive model aero engine lean burn injection system. Experimental Thermal and Fluid Science 52:164-173.

[14] Cafiero G, Ceglia G, Discetti S, Ianiro A, Astarita T and Cardone G (2014b) On the three-dimensional precessing jet flow past a sudden expansion. Experiments in Fluids 55:1677.

[15] Greco CS, Ianiro A, Astarita T and Cardone G (2013) On the near field of single and twin circular synthetic jets. International Journal of Heat and Fluid Flow 44:41-52.

[16] Zhou DW, Lee SJ (2004) Heat transfer enhancement of impinging jets using mesh screens. International Journal of Heat and Mass Transfer 47: 2097-2108.

[17] Zhou DW, Lee SG, Ma CF, Bergles AE (2006) Optimization of mesh screen for enhancing jet impingement heat transfer. Heat and Mass Transfer 42: 501-510.

[18] Lee DH, Lee YM, Kim YT, Won SY, Chung YS (2002) Heat transfer enhancement by the perforated plate installed between an impinging jet and the target plate. International Journal of Heat and Mass Transfer 45:213-217.

[19] Cafiero G, Discetti S and Astarita T (2014a) Heat transfer enhancement of impinging jets with fractal-generated turbulence. International Journal of Heat and Mass Transfer 75: 173-183.

[20] Hurst D and Vassilicos JC (2007) Scaling and decay of fractal-generated turbulence. Physics of Fluids 19: 035103.

[21] Mazellier N, Vassilicos JC (2010) Turbulence without Richardson-Kolmogorov cascade. Physics of Fluids 22: 075101.

[22] Geipel P, Goh KHH, Lindstedt RP (2010) Fractal-generated turbulence in opposed jet-flows. Flow Turbulence and Combustion 85-397-419.

[23] Kinzel M, Wolf M, Holzner M, Lüthi B, Tropea C, Kinzelbach W (2011) Simultaneous two-scale 3D-PTV measurements in turbulence under the influence of system rotation. Experiments in Fluids 51:75–82.

[24] Nedic J, Ganapathisubramani B and Vassilicos JC (2012) Aeroacoustic Perfromance of Fractal Spoilers. AIAA Journal 50(12):2695-2710.

[25] Astarita T (2007) Analysis of weighting windows for image deformation methods in PIV. Experiments in Fluids 46: 1115-1123.

[26] Wieneke B (2008) Voulme self-calibration for 3D particle image Velocimetry. Experiments in Fluids 45: 549-556.

[27] Discetti S and Astarita T (2014) The detrimental effect of increasing the number of cameras on self-calibration for tomographic PIV. Measurement Science and Technology 25(8): 084001

[28] Elsinga GE, Scarano F, Wieneke B and van Oudheusden BW (2006) Tomographic particle image velocimetry. Experiments in Fluids 41:933-947.

[29] Novara M and Scarano F (2012) Performances of motion tracking enhanced Tomo-PIV on turbulent shear flows.

[30] Discetti S, Natale A and Astarita T (2013) Spatial Filtering Improved Tomographic PIV. Experiments in Fluids 54:1505.

[31] Discetti S and Astarita T (2012) Fast 3D PIV with direct sparse cross-correlations. Experiments in Fluids 53:1437-1451

[32] George WK (1992) The decay of homogeneous isotropic turbulence. Physics of Fluids 4:1492.

[33] Valente PC, Vassilicos JC (2011) The decay of turbulence generated by a class of multiscale grids. Journal of Fluid Mechanics 687: 300-340.